mater.scichina.com link.springer.com

Published online 11 March 2022 | https://doi.org/10.1007/s40843-021-1973-y
Sci China Mater 2022, 65(7): 1727–1740

Nanophotonic-structured front contact for high-performance perovskite solar cells

Md. Akhtaruzzaman[1,3,4†*], Mohammad Ismail Hossain[2,8†*], Mohammad Aminul Islam[5,9], Md. Shahiduzzaman[6], Ghulam Muhammad[7], A. K. Mahmud Hasan[1*], Yuen Hong Tsang[2] and Kamaruzzaman Sopian[1]

ABSTRACT **We report the design of a nanophotonic metal-oxide front contact aimed at perovskite solar cells (PSCs) to enhance optoelectronic properties and device stability in the presence of ultraviolet (UV) light. High-quality Cr-doped ZnO film was prepared by industrially feasible magnetron sputter deposition for the electron transport layer of PSCs. As a means, the influence of the Cr content on the film and device was systematically determined. In-depth device optics and electrical effects were studied using advanced three-dimensional opto-electrical multiphysics rigorous simulations, optimizing the front contact for realizing high performance. The numerical simulation was validated by fabricating PSCs optimized to reach high performance, energy conversion efficiency (ECE) = 17.3%, open-circuit voltage (V_{OC}) = 1.08 V, short-circuit current density (J_{SC}) = 21.1 mA cm^{-2}, and fill-factor (FF) = 76%. Finally, a realistic front contact of nanophotonic architecture was proposed while improving broadband light absorption of the solar spectrum and light harvesting, resulting in enhanced quantum efficiency (QE). The nanophotonic PSC enables J_{SC} improvement by ~17% while reducing the reflection by 12%, resulting in an estimated conversion efficiency over 23%. It is further demonstrated how the PSCs' UV-stability can be improved without considerably sacrificing optoelectronic performances. Particulars of nanophotonic designed ZnO:Cr front contact, PSCs device, and fabrication process are described.**

Keywords: ZnO:Cr front contact, magnetron sputtering, perovskite solar cells, UV stability, optics and electrical effects

INTRODUCTION

The photovoltaic research community has paid great attention to perovskite solar cells (PSCs) in correspondence to their significant energy conversion efficiency (ECE) advancement (from 3.8% to 25.5%) in just a few years [1–4]. The direct and tunable bandgap, extended light absorption profile, carrier lifetime, long space charge region in the micrometer scale, defect tolerance factor, high carrier mobility, and straightforward deposition possibilities are major attributes that make the perovskite material even so elegant for various optoelectronic device applications [5–8]. The organic-inorganic framework of the perovskite material system allows realizing high-efficiency PSCs as well as tandem solar cells (TSCs) [9–13]. The electron transport layer (ETL) of PSCs shows significant importance in attaining efficient photogenerated electron withdrawal and transportation to the corresponding electrode [14,15]. The ETL and perovskite absorber interface demonstrate significant importance in device performance and stability [6,15]. Hence, efficient electron transport material selection, extending PSCs' photovoltaic performance and stability, is a contemporary demand. Recently, several metal oxides, such as TiO_2, ZnO, and SnO_2, have demonstrated immense performances as ETLs for realizing single-junction PSCs [14–16] and perovskite-based TSCs [12,17,18]. In conventional PSC fabrication, TiO_2 and SnO_2 are most widely considered as potential ETLs owing to their suitable energy level and transparency [19,20]. However, both transport materials have some shortcomings that restrict the efficient device fabrication with improved stability. TiO_2 gets unstable under ultraviolet (UV) light while exhibiting poor carrier mobility, high charge trapping location, and high charge accumulation within the layer junction [19,21].

On the other hand, deployment of SnO_2 in PSC fabrication allows improving device stability with superb carrier mobility; nevertheless, unfavorable hysteresis consequences limit the high conversion efficiency [20]. ZnO has latterly been considered a potential electron transport material due to its high optical transparency, suitable work function, flexibility, and superior

[1] Solar Energy Research Institute (SERI), Universiti Kebangsaan Malaysia, 43600 Bangi, Selangor, Malaysia
[2] Department of Applied Physics, Hong Kong Polytechnic University (PolyU), Kowloon, Hong Kong, China
[3] Centre for Integrated Systems Engineering and Advanced Technologies (Integra), Faculty of Engineering and Built Environment, Universiti Kebangsaan Malaysia (UKM), 43600 Bangi, Selangor, Malaysia
[4] Graduate School of Pure and Applied Sciences, University of Tsukuba, Tsukuba, Ibaraki 305-8573, Japan
[5] Department of Electrical Engineering, Faculty of Engineering, University of Malaya, Jalan Universiti, 50603 Kuala Lumpur, Selangor, Malaysia
[6] Nanomaterials Research Institute (NanoMaRi), Kanazawa University, Kakuma, Kanazawa 920-1192, Japan
[7] Department of Computer Engineering, College of Computer and Information Sciences, King Saud University, 11543 Riyadh, Saudi Arabia
[8] Department of Electrical and Computer Engineering, University of California, Davis, CA 95616, USA
[9] Institute of Sustainable Energy, Universiti Tenaga Nasional (@The National Energy University), Jalan IKRAM-UNITEN, 43000 Kajang, Selangor, Malaysia
† These authors contributed equally to this work.
* Corresponding authors (emails: akhtar@ukm.edu (Akhtaruzzaman M); mihossain@ucdavis.edu (Hossain MI); mahmud.1st@gmail.com (Hasan AKM))

carrier mobility, which can overcome the constraints mentioned above for realizing efficient PSCs [5,22,23]. Several solution and vacuum deposition routes can prepare ZnO films (e.g., spin coating, spray pyrolysis, sol-gel and sputtering, chemical vapor deposition, electron beam deposition, and atomic layer deposition) [16,24,25]. Numerous attempts have been made so far for improving the optoelectronic parameters of ZnO in many forms, such as amorphous, crystalline, or nanostructured [26]. One possible way to increase the conductivity by maintaining a trade-off with ZnO film's transparency is by doping with suitable dopants (e.g., Al, B, and Sn) [22,27]. It has been demonstrated that the doped ZnO exhibits better photophysical properties than the intrinsic ZnO, which are beneficial for realizing high-efficiency photovoltaic or sensor devices [28,29]. Deposition conditions and dopant concentrations also demonstrate a critical part of film's optoelectronic properties. A superficial neutralization with MgO thin film and protonated ethanolamine (EA) turns ZnO into a very encouraging ETL for delivering hysteresis-free and efficient PSCs *via* regulating the surface dipole, leading to improved electron transportation kinetics, ensuing hysteresis-free ECE of 21.1% for the champion PSC device [30].

Furthermore, ZnO's passivations by Cl (ZnO-Cl) and S (ZnO-ZnS) are realized over easy chemical interchange tactics, attaining an ECE of over 20%. Additionally, sulfur present on the ZnS surface binds coordinately at the Lewis acid site of Pb, thereby showing excellent UV solidity [31,32]. Additionally, Nb_2O_5 treatment of the surface can also passivate chemical uncertainty [7]. Zheng *et al.* [33] manufactured a ZnO ETL through a $Zn(NO_3)_2$ combustion route, resulting in a self-passivating surface with partial contaminations and a small presence of hydroxyl functional groups, achieving an ECE of 19.84% with inhibited hysteresis as well as high ambient and thermal firmness. Liang *et al.* [34] proposed the preparation of ZnO ETL *via* the sol-gel method with a stabilizing ligand mono-EA. The existence of ligands likewise extraordinarily changed the work function of related ZnO films, thus causing an incredibly diverse impact on the device's performance [30,35]. So far, boron- and aluminum-doped ZnO materials are commonly used in PSCs [16,22]; however, to the best of our knowledge, no significant contribution of ZnO:Cr transport material in PSCs is yet thoroughly investigated.

The current research primarily concentrates on the preparation and characterization of the Cr-doped ZnO material. We aim to make high-quality ZnO:Cr film as a potential ETL suitable for efficient PSCs. The magnetron sputter deposition technique is used to deposit the film at room temperature. We investigate the influence of deposition factors, particularly chromization, on the deposited ZnO:Cr film's physical, morphological, and optoelectronic virtues. We study the prospect of using ZnO:Cr as ETL for efficient PSCs by employing an advanced opto-electrical three-dimensional (3D) electromagnetic simulation which is composed of finite-difference time-domain (FDTD), finite element method (FEM) in addition with particle swarm optimization (PSO) algorithm. Additionally, an efficient PSC device is fabricated to validate the adapted numerical approach. Finally, we design and propose a nanophotonic PSC that can exhibit efficient photon management and better charge extraction, resulting in high ECEs and better UV stability. Comprehensive information on film preparation, PSC fabrication, optimization, and optoelectrical characteristics are discussed in the following sections.

EXPERIMENTAL SECTION

Film preparation and device fabrication

The ZnO:Cr films were prepared by magnetron sputtering on a glass substrate using ZnO (99.99%) and Cr (99.99%) targets consecutively in Ar (pure) environment. The chamber working pressure was sustained at 2.7×10^{-2} Torr (1 Torr = 133.3 Pa) during the deposition period. Before the deposition, 30 mm × 30 mm glass substrates were washed with sonication in soap water and then in acetone, followed by a wash in ethanol, and lastly, de-ionized water for 10 min in each medium. The clean substrates were then dried with dry nitrogen gas. The substrate holder was set to be 14 cm apart from the target. The deposition was performed at room temperature, confirmed by installing a thermocouple integrated with the chamber cooling arrangement. The ZnO was deposited at an optimized fixed radio frequency (RF) power of 50 W while direct current (DC) power was varied from 0 to 30 W for ZnO:Cr film formation. The reactive gases of ultrapure (5 N) argon were inserted at 4 sccm (1 sccm = 1 $cm^3\ min^{-1}$). The Supplementary information (Section S1) describes the characterization of the thin films. In PSC fabrication, the glass/fluorine-doped tin oxide (FTO) substrates were cleaned at the very beginning. Priorly patterned and sized substrates were successively cleaned with potassium hydroxide (KOH) solution (1.4 g KOH in 50 mL ultrapure water) in a sonication bath for 10 min. After that, the substrates were again poured into only ultrapure water in a sonication bath for 10 min twice. More details on the experimental information of fabricated devices and characterization can be found in the previous work [4].

Numerical simulation and modeling method

A combined opto-electrical 3D numerical simulation approach was considered to investigate the PSCs. The proposed PSC optics optimization was performed by the FDTD technique integrated with the PSO algorithm. The input parameters for such setup were achieved by optical characteristics of the proposed materials. Fig. S1 in the Supplementary information represents the complex refractive indices of used materials, either determined through ellipsometry measurement or considered from previous studies [28]. Besides, the FEM simulation was carried out to determine the device's current-voltage (*J*-*V*) characteristics, which further allow realizing photovoltaic parameters of solar cells. Necessary electronic parameters of the used materials are listed in Table S1. A comprehensive description to calculate the time-average power density, quantum efficiency (QE), short-circuit current density (J_{SC}), and *J*-*V* characteristics is available in the literature [8,13,36].

RESULTS AND DISCUSSION

Realization of high-quality ZnO:Cr thin-films

A systematic analysis of the deposited ZnO:Cr thin films was carried out for the deposition power of 0, 5, 10, 20, and 30 W. The influence of the Cr dopant on the undoped ZnO film was investigated by analyzing structural, morphological, electrical, optical, and compositional properties. The film thickness varied from 15 to 40 nm while the deposition power changed from 0 to 30 W. The surface morphology of intrinsic ZnO and ZnO:Cr

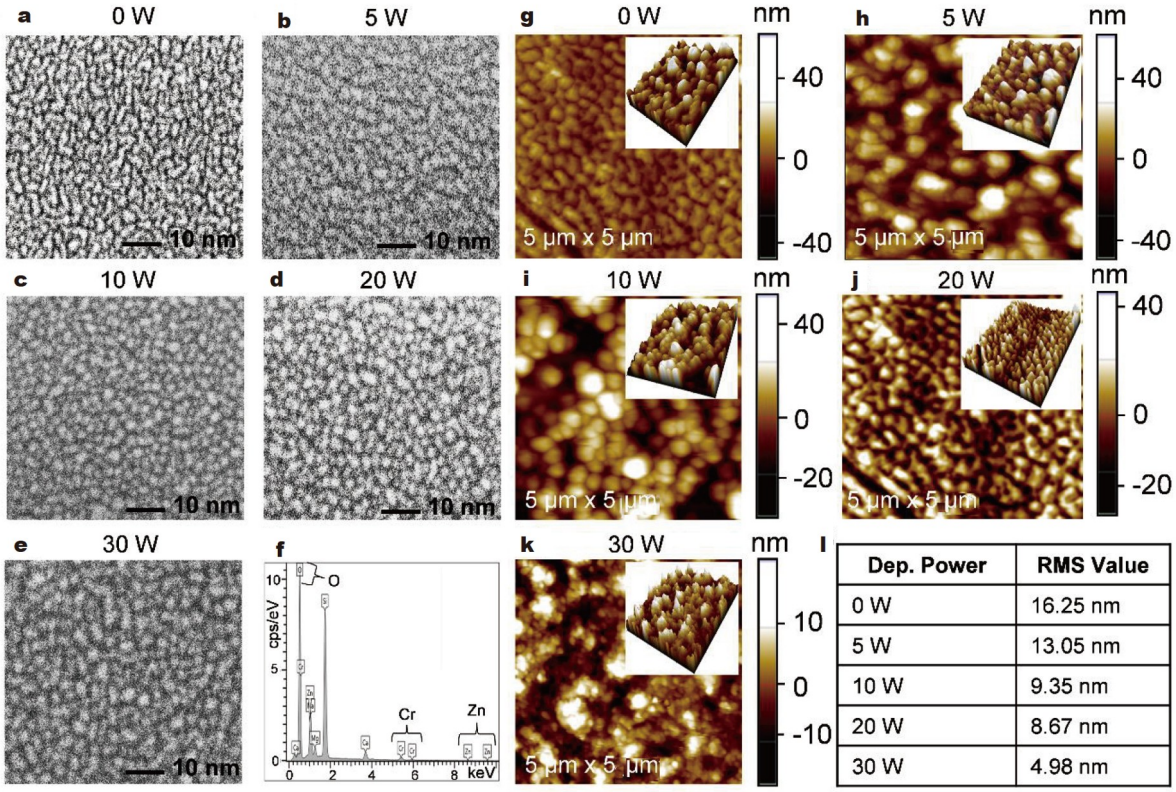

Dep. Power	RMS Value
0 W	16.25 nm
5 W	13.05 nm
10 W	9.35 nm
20 W	8.67 nm
30 W	4.98 nm

(f1)	0 W	5 W	10 W	20 W	30 W
Cr (wt%)	0	2.21	4.04	10.62	15.36
Zn (wt%)	22.38	20.38	19.81	17.02	16.61
O (wt%)	77.62	77.41	76.15	72.36	68.03

Figure 1 FESEM images of the prepared ZnO:Cr thin-film for the deposition powers of (a) 0 W (undoped ZnO), (b) 5 W, (c) 10 W, (d) 20 W, and (e) 30 W with x = 350 K and working distance = 2.4 mm. (f) EDX spectra of the ZnO:Cr with the deposition power of 20 W (the weight percentages for Zn, O, and Cr are shown in (f1) table upon eliminating other elements). Atomic force microscopy (AFM) images of the ZnO:Cr thin-film for the deposition powers of (g) 0 W (undoped ZnO), (h) 5 W, (i) 10 W, (j) 20 W, and (k) 30 W. (l) The RMS surface roughness of the individual case shown in (g–k).

nanoparticles at different deposition powers are presented in Fig. 1a–e. Fig. 1a demonstrates the random grain distribution in the case of pure ZnO nanoparticles; however, with the increase of the percentage of Cr doping (power changed from 0 to 30 W), the film assembly of ZnO:Cr nanocrystals fluctuates from undoped ZnO nanocrystals. The insertion of Cr changes the grain shape from disrupted to spherical and distributed consistently, covering the entire glass substrate without creating a pinhole, as shown in Fig. 1b–e. Noticeably, the ZnO:Cr film exhibits distinct morphology in each variation of the Cr deposition power due to different Cr percentages in the film. The energy dispersive X-ray spectroscopy (EDX) measurement was conducted to further analyze the elemental commotion, and the results are presented in Fig. 1f, confirming the primary composition of Cr, Zn, and O elements. A change in the elemental composition of Cr, Zn, and O species demonstrates the impact of deposition power on the ZnO:Cr film. The presence of Ca, Si, and Mg in the film can also be traced from the EDX spectrum originating from the glass substrate.

Surface analytical images of the deposited ZnO:Cr film for various Cr deposition powers are illustrated in Fig. 1g–k. The root-mean-square (RMS) value deviates from 16.25 to 4.98 nm while changing the Cr deposition power from 0 to 30 W (Fig. 1l). The reduction of RMS roughness ensures the uniformity and compactness of the deposited film. The phenomena can also be validated by field emission scanning electron microscopy (FESEM) images and the X-ray diffraction (XRD) patterns, as presented in Figs 1 and 2a. Such an occurrence is advantageous for sidestepping different trap densities, acting as carrier recombination centers in a photovoltaic device. The structural and crystallinity phases of the prepared ZnO:Cr films depend on various DC gun powers studied through the XRD measurement for the angular region from 10° to 70°, as shown in Fig. 2a. It is observed that all major peaks are available from the undoped ZnO films, which are ascribed to the crystal planes (100), (002), (101), (102), (110), (103), and (112) [37]. It is noticed that the increase in deposition power significantly influences the crystallinity of the deposited film, where no peak was observed for 30 W, indicating the amorphous nature of the film. The existence of Cr without showing any phase of Cr-doped ZnO nanoparticles was validated by the EDX measurement, which further confirms that Cr^{3+} has penetrated the ZnO frameworks by replacing Zn^{2+}, introducing defect states nearby the dopant into the crystal [38]. With the integration of Cr^{3+}

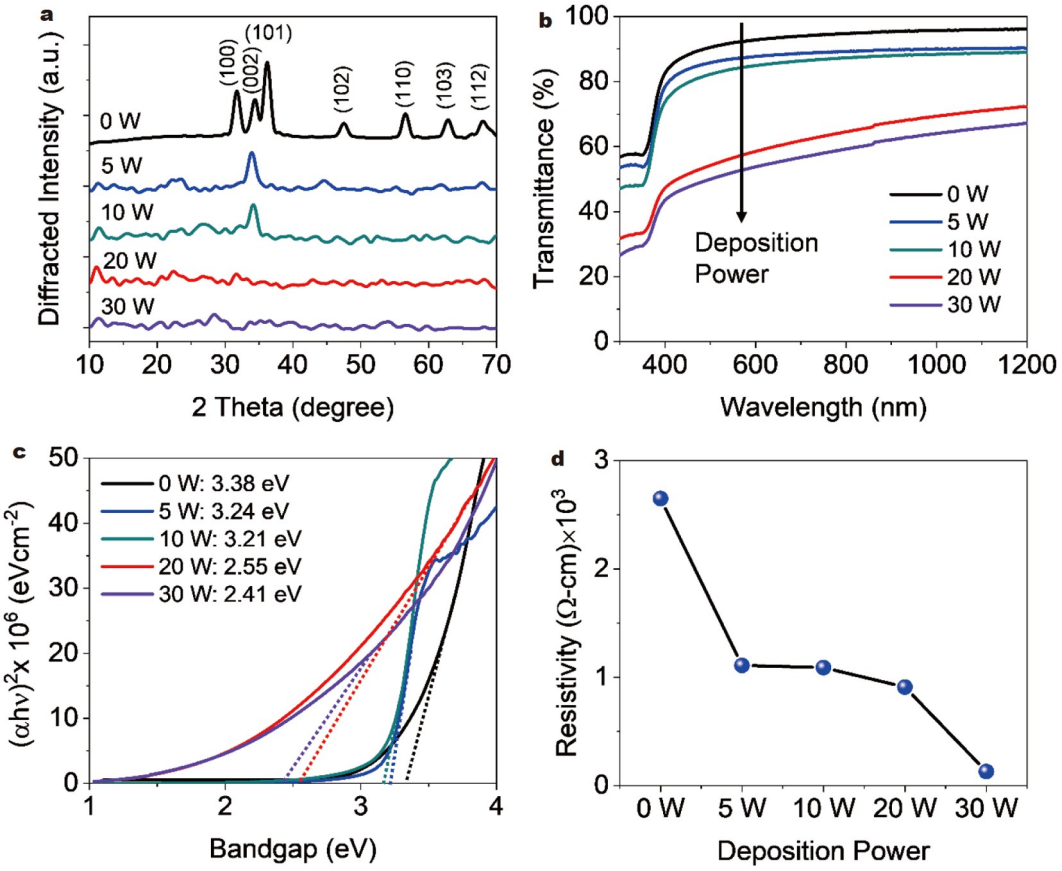

Figure 2 The Cr deposition power-dependent (a) XRD patterns, (b) optical transmittance, (c) absorption coefficient with bandgap determination, and (d) resistivity of ZnO:Cr films.

within the ZnO wurtzite configuration, Cr^{3+} might take placement into two different sites on the ZnO matrix. Cr^{3+} can occupy the interstitial positions of ZnO as defects in octahedral coordination, or preferably the Zn^{2+} is substituted by Cr^{3+}, providing increased electronic attributes of the pristine ZnO material, producing more charge carriers [39]. The O^{2-} 2p states are responsible for the upper valence band (VB) of ZnO. But, the Zn^{2+} 4s states determine the lowest conduction band (CB) on ZnO [40]. The continuous increment of Cr^{3+} fusion into ZnO causes a lowering of the bandgap energy (E_g) of subsequent structures. Because the Cr^{3+} 3d states take charge to create the lowest CB instead of Zn^{2+} 4s in ZnO:Cr matrix once Cr^{3+} ions are incorporated into ZnO framework, which causes lowering conduction band minima (CBM) [39]. The optical properties also certify the same outcome as a means of higher absorption in the visible region of the spectrum [41]. On the other hand, the n-type properties of ZnO:Cr is the outcome of shifted Fermi level (E_F) upward due to Cr^{3+} integration in ZnO. The peak concerning the (002) plane shows a dominating characteristic (higher intensity) than other XRD peaks, which also disappears while the deposition power is over 10 W. The development of *c*-axis directional film might be originated from the existence of a dipole moment. The exchange of smaller-sized Cr^{3+} with Zn^{2+} ions also causes expansion of lattice parameters to shift the XRD peaks towards a lower 2θ angle [42]. The extended peaks show that Cr's insertion into the ZnO lattice degrades the polycrystalline film's crystallinity. The ionic radius of Cr is lower than that of Zn, which causes lattice damage in the form of compressive strain (Zn replaces Cr) or tensile strain (Cr replaces Zn), promoting the amorphous polycrystalline film. The deposited film's optical properties were studied by the UV-visible measurement, which allows determining absorption spectra and optical transparency. The influence of the deposition power on the ZnO:Cr film's transparency is illustrated in Fig. 2b for the wavelength range of 300–1200 nm. The films with lower Cr concentrations exhibit optimal transparency (>90%) in the visible-infrared range; however, an increase of Cr deposition power leads to minimizing the film transparency. In the case of 30 W, the transmission drops significantly, and it is confirmed that the film is not suitable for photovoltaic applications. The phenomena are opposite for the absorption spectra, where a high absorption is achieved in the case of high deposition power shown in the absorption coefficient plot in Fig. 2c. The bandgap of the ZnO:Cr can also be estimated from the absorption coefficient plot by defining a Tauc relation ($\alpha h\nu = A(h\nu - E_g)^n$), where α represents the absorption coefficient, the photon energy and optical bandgap are denoted by $h\nu$ and E_g, respectively, and A is a constant. The 'n' is dependent on the transition type—1/2, 2, 3/2, and 3 for direct, indirect, forbidden direct, and forbidden indirect transitions, respectively.

ZnO:Cr is a direct bandgap material; thus, n = 1/2 was considered for the bandgap extrapolation. The bandgaps of films are calculated to 3.38, 3.24, 3.21, 2.55 and 2.41 eV for the case of 0, 5, 10, 20, and 30 W, respectively. The calculated absorption coefficient and E_g values exhibit incremental absorption at the lower wavelength region of the solar spectrum due to the higher

penetration of Cr content into the lattice. This happens while the Cr^{3+} doping takes place into the ZnO matrix in a substitutional and interstitial way. In the substitutional route, Cr^{3+} replaces Zn^{2+} in ZnO. On the other hand, Cr^{3+} occupies the interstices in the structure. The absorption profile of lower-Cr-content ZnO:Cr film is also lower since substitutional doping has occurred. But at higher Cr contents in ZnO:Cr, Cr assembles at interstitial sites of ZnO lattice, leading to higher absorption [43]. The literature shows that E_g values of intrinsic ZnO thin films vary within 3.25–3.39 eV [44,45]. However, the E_g of ZnO decreases while Cr is inserted in the lattice [46]. This reduction in E_g of ZnO:Cr may be due to the sp-d orbital rotation altercation in the interface between CB electrons and the d electrons of Cr^{3+}, resulting in decreasing CBM edge and a rise in valence band maxima (VBM) [47,48]. The responsiveness towards visible light of Cr-doped ZnO thus occurs eventually by this shortened E_g. The E_g is inversely in response to grain size in a thin film. The FESEM of the current study also reveals that bigger grains in the presence of more Cr lead to reduced E_g. This means that the ratio of the compositional element existing in the ZnO:Cr film significantly dominates the corresponding E_g and variation in the crystallographic phase and orientation. The films' resistivity (ρ) is shown in Fig. 2d, varying from 2.65 to 0.13 kΩ cm by varying the deposition power from 0 to 30 W. Table 1 summarizes the carrier mobility (μ) and carrier concentration values of the prepared films. The μ, resistivity, and carrier concentration are essential electrical properties that control the charge transferring attributes of semiconductors while being incorporated as an ETL to realize high-performance PSCs. High mobility and high conductivity are prerequisites for efficient charge transfer; however, there is always a trade-off between optical and electrical parameters that need to be maintained for designing the efficient optoelectronic device.

For example, it is evident that by increasing the Cr doping, the conductivity and carrier mobility are significantly improved; on the other side, the film's optical transparency considerably drops, which does not allow for a potential charge carrier (electron) material for PSC solar cells. In this study, electron concentrations were found in the range of 9.1×10^{14} to 4.04×10^{17} cm^{-3}, while a similar observation was seen from the published work on the sputtered a-ZTO (zinc tin oxide) films by Rajachidambaram *et al.* [49]. The μ of the ZnO:Cr films is on the scale of 6.32–50.2 $cm^2\ V^{-1}\ s^{-1}$ in the case of undoped and ZnO:Cr films. The lower μ implies the higher carrier concentration, shown in Table 1. As the metallic contents (Cr) increased, the film became amorphous at higher RF power, leading to increased dislocation density and lattice defects, and thus reduced mobility. The deficiency of oxygen and Cr-rich states may create such defects, as validated by the contentious decrement of O_2 content. The above investigation of the deposited ZnO:Cr films clearly indicates the effect of Cr doping on the ZnO material characteristics. Using the ZnO:Cr film as a potential ETL to realize PSCs, the film should provide a uniform surface, compactness, high transparency, high conductivity, high carrier mobility, and low absorption. However, it is not easy to fulfill all ETL requirements. Several factors have to be considered to minimize the trade-off in optoelectronic properties of an ETL. In the later subdivision, we will investigate the incorporation of ZnO:Cr film as an ETL in PSCs for different deposition powers and their corresponding impact on the device ECE.

Table 1 Electronic properties of the prepared ZnO:Cr films deposited by co-sputtering technique while varying the deposition power

Deposition power (W)	Mobility ($cm^2\ V^{-1}\ s^{-1}$)	Carrier concentration ($\times 10^{16}$ cm^{-3})
0	50.2	0.091
5	11.4	1.35
10	8.91	6.26
20	6.32	20.76
30	3.52	40.42

PSCs: Structure, fabrication, and validation

Typically, PSCs follow either a superstrate or substrate architecture. A superstrate architecture starts by easily depositing device constituents on a transparent conducting oxide (TCO) substrate such as FTO and indium tin oxide (ITO). In comparison, substrate architecture allows the fabrication of solar cells on different plastic or flexible substrates [15,28]. This device structure additionally permits the fabrication of highly efficient TSCs where PSC is used as a top cell in the multijunction tandem structure [10–12,29]. The perovskite active layer is sandwiched between charge-carrier layers such as ETL and hole transfer layer (HTL) in case of both types of device fabrication. The present study aims to fabricate effective PSC in superstrate architecture so that the experimental output could offer an important reference and approval of our numerical approach. An 80-nm TiO_2 ETL was deposited on an FTO-glass substrate while fabricating PSC. A ~300-nm $MAPbI_3$ active layer and 250-nm HTL were deposited on the ETL. The TiO_2 was optimized using compact-layer (CL) or bilayer TiO_2 and mesoporous (mp)-TiO_2 layer for achieving high efficiency. In the end, a ~100-nm-thick Au back contact was deposited through the resistive thermal evaporator to finish the full device fabrication. To understand the potential of using ZnO:Cr as an ETL, we replaced the TiO_2 by ZnO:Cr and spiro-OMeTAD by a double NiO/ZnO layer in the simulation study, which can also benefit the device's stability due to inorganic transporting materials [28,50]. In this study, we used a thin (~10-nm) NiO layer combined with a 200-nm ZnO layer to make the HTL, resulting in several advantages, such as high carrier mobility, high conductivity, good chemical robustness, and efficient carrier collection from the $CH_3NH_3PbI_3$ layer [10,51]. A schematic of the ZnO:Cr-ETL (Planar Structure B)-based PSC is shown in Fig. 3a, with related energy levels in Fig. 3b. The superstrate PSC can exhibit high efficiency and high stability due to incorporating inorganic transporting materials; however, such devices cannot exhibit adequate spectral response for possessing a planar front contact scheme causing incident light reflection. This phenomenon leads to a substantial loss in J_{SC} or ECE. Thus, as a final step of this study, we propose a nanophotonic front contact design for PSCs in substrate configuration, which can overcome such limitations and allow high efficiency. The proposed PSC covered with nanotextured front contact attributed to enhanced light penetration and trapping, thereby contributing better carrier mining, leading to improved open-circuit voltage (V_{OC}) and fill-factor (FF). Detailed information on the proposed device structural design and optimization method are discussed in the section of "Nanophotonic design of PSCs". In PSC fabrication, the underlying layer of the perovskite absorber has an immense impact on forming high-quality perovskite film [52], which

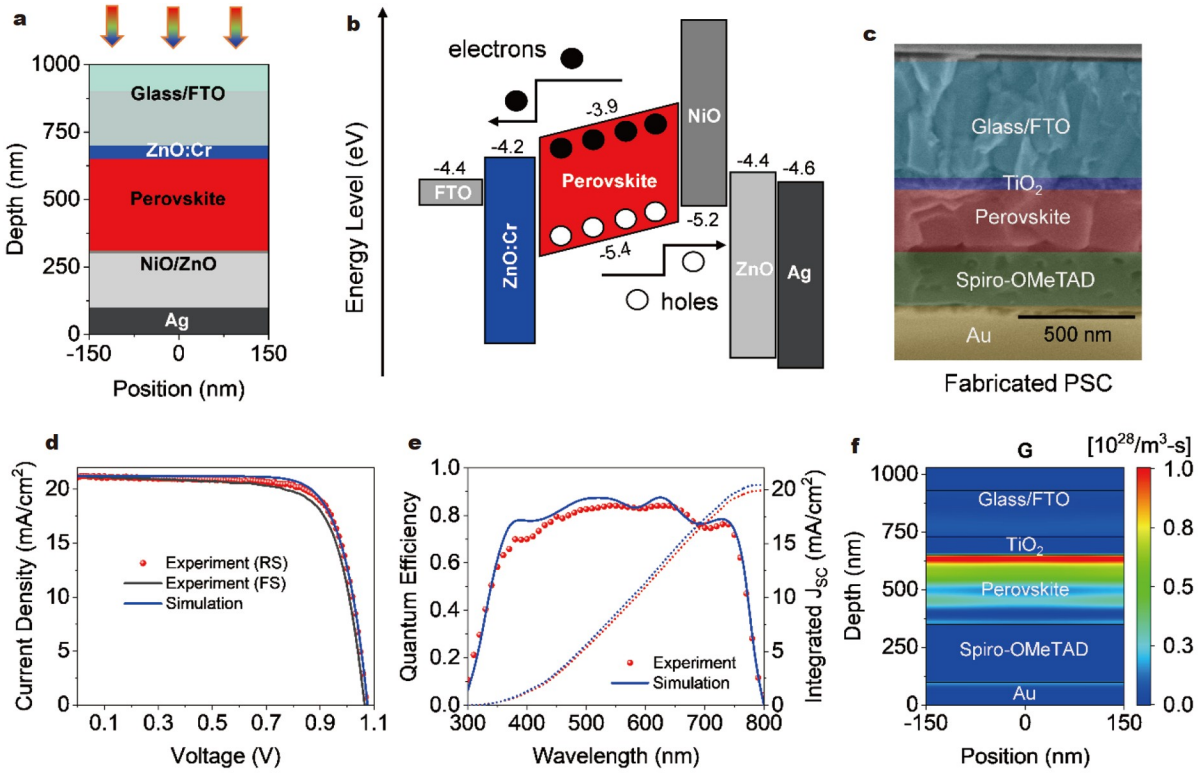

Figure 3 (a) Schematic of the PSC in superstrate configuration with ZnO:Cr as an ETL and (b) corresponding energy levels. (c) The CR SEM image of PSC fabricated in superstrate architecture. (d) A comparison of *J-V* between experimental and numerical simulation results. (e) Comparison of the fabricated and simulated devices' QEs and integrated J_{SC}. (f) The total generation rate (*G*) of the simulated PSC.

further promotes a high-performance device. Hence, we deposited the perovskite ($MAPbI_3$) film on an optimized TiO_2 ETL/FTO substrate to ensure high performance. A cross-sectional (CR) SEM image of the fabricated PSC (Planar Structure A) with the device configuration FTO/TiO_2 CL/mp-TiO_2/$MAPbI_3$/spiro-OMeTAD/Au is shown in Fig. 3c. The *J-V* characteristics and QE of the fabricated PSC are presented in Fig. 3d, e, respectively.

The PSC exhibits a J_{SC} of 21.1 mA cm^{-2}, V_{OC} of 1.08 V, FF of 76%, and ECE of 17.3% with the reverse scan (RS). Meanwhile, J_{SC} of 21.2 mA cm^{-2}, V_{OC} of 1.07 V, FF of 73%, and ECE of 16.4% are pronounced at forward scan (FS). All extracted photovoltaic parameters are presented in Table 2. The PSC displays a high QE over the 300–800 nm spectral region, especially, ~80% in the high energy segment of the solar spectrum, as shown in Fig. 3e. The cumulative J_{SC} was 20 mA cm^{-2}. Most UV light (<360 nm) is captivated principally at the ETL, eventually not contributing to improving J_{SC}. However, 400–700 nm photons are completely harvested by the $CH_3NH_3PbI_3$ layer. Incident light has a great impact on device stability. The light soaking stability (light stability) of the fabricated PSC was performed and included in the Supplementary information (Fig. S2). The measurement was performed under 1 sun illumination for ~150 min in an atmospheric environment, with a humidity range of 30%–40%, for evaluating the reliability of the fabricated device. After the light stability test, the resultant device retained almost 65% of its initial conversion efficiency, as shown in Fig. S2d. Also, the resulting PSC showed a few noticeable breakdowns in J_{SC}, and V_{OC} even after 150 min continuous light exposure (Fig. S2a, b). Maximum power point tracking (MPPT) was considered for evaluating steady-state J_{SC} (Fig. S3), notifying that steady-state J_{SC} with bias voltage (V_{max}) is 0.88 V at AM 1.5G illumination. The stabilized ECE of ~17.1% is close to that obtained from the *J-V* curve of the fabricated device.

Moreover, like many other factors, UV-induced degradation is one reason that affects PSC stability. The UV stability issue originates from the establishment of heterojunctions between ETL-perovskite and perovskite-HTL; hence, an efficient ETL can improve the UV-stability of PSCs [53–55]. In this study, we attempt to consider Cr-doped ZnO as an ETL for PSCs, which can improve the UV stability of PSCs due to their excellent optoelectronic properties and chemical stability. The EXPERIMENTAL SECTION provides further particulars on optimization, materials for full device fabrication, the process of device fabrication, and corresponding characterization. The current investigation is mostly for motivating optoelectronic characteristics realized through the advanced FDTD-FEM method that examines optical and electrical enactments of a solar cell. FDTD simulations confirm outstanding settlement amongst the experimental and measured QEs (Fig. 3e). In particular, spectral wavelengths below 360 nm and over 750 nm are well defined through the FDTD study. The as-supplied FTO has a rough surface; hence, a pyramid-shaped rough FTO surface in the unit cell with a low profile dimension (period and height of 600 and 70 nm, respectively) was considered in optical simulations to provide realistic information. The 3D FDTD simulations deliver a genuine photon absorption profile of a unit cell since it considers the experimentally realized materials' optical constants (Fig. S1). However, FDTD analysis does not result directly in the electrical performance of the device, which is desirable for a

comprehensive understanding of the studied solar cell. Consequently, the combined FDTD-FEM method used in the current study allows revealing *J-V* characteristics while taking optical information input in terms of generation rate (*G*) of the absorber. The total electron-hole generation rate was determined from optical simulations and presented in Fig. 3f. It is clearly observed that the *G* is higher near the vicinity of TiO_2 and perovskite layers. FEM simulation takes individual material's electronic properties as an input parameter recorded in Table S1. Further evidence about the arithmetical simulation process is described in the EXPERIMENTAL SECTION and elsewhere in earlier investigation [5,21,36]. The mutual FDTD-FEM methodology nicely confirms the investigational *J-V* output, as expressed in Fig. 3d. The study of the proposed PSC's device performance through coupled simulation delivers a 21.3 mA cm^{-2} of J_{SC}, 1.08 V of V_{OC}, 76% of FF, and 17.5% of ECE. Interestingly, those values mimic the photovoltaic presentation of a real-time fabricated device (Table 2). It is also expected that the device's performance can be improved by maintaining the perfection of interfaces between perovskite and contacts. It is good to observe that the simulation can authorize the electrical properties of a real device, offering a pathway in optimizing future PSC devices for determining high efficiency. Specifically, the reflection loss of incident light occurs at the front contact due to its planer surface morphology in the fabricated device. Here we aim to design the nanophotonic front contact by 3D FDTD simulation to optimize the PSC for better optoelectronic performance in terms of efficient photon management.

Influence of Cr doping on the device performance

This section investigates the influence of deposition power (Cr content) for the ZnO:Cr film on the PSC performance considering the device structure illustrated in Fig. 3a. Understanding the optimum deposition power for determining the ZnO:Cr ETL for efficient PSCs is essential. We investigate the optoelectronic performance of PSCs while varying the deposition power of the ZnO:Cr ETL. The deposited ZnO's complex refractive index for various deposition powers was calculated through spectroscopy measurement, provided in Fig. S1a, c. The ZnO:Cr front contact greatly influences the optics of the complete solar cell. Fig. 4a, b show the calculated QE and parasitic losses of PSCs for various deposition powers. An increase of the deposition power leads to a decrease in the photon absorption (or increase in the ZnO:Cr absorption) only in the shorter wavelength region (300 to 500 nm). No significant influence of

Table 2 Comparative photovoltaic values deduced from *J-V* curves shown in in Fig. 3d

Type	V_{OC} (V)	J_{SC} (mA cm^{-2})	FF (%)	ECE (%)
Experiment (RS)	1.08	21.1	76	17.3
Experiment (FS)	1.07	21.2	73	16.4
Simulation	1.08	21.3	76	17.5

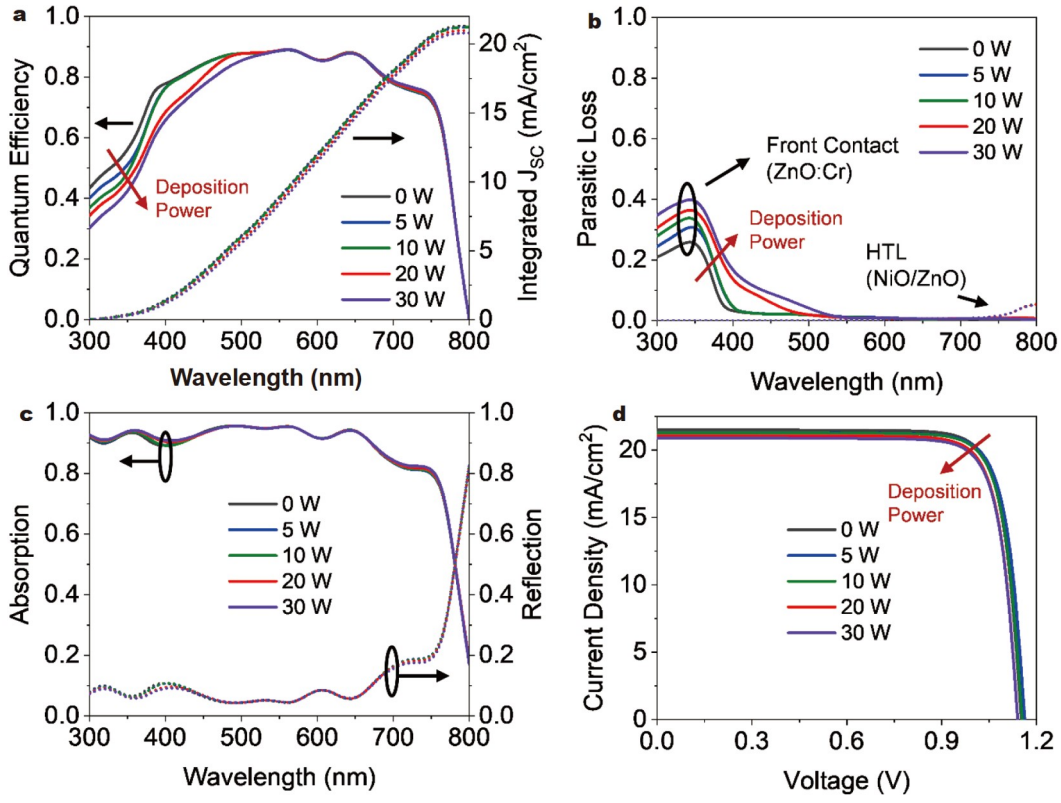

Figure 4 A comparison of calculated (a) QEs and integrated J_{SC}, (b) parasitic absorptions, (c) total absorptions, and reflections for the PSCs with various deposition powers. (d) A comparison of *J-V* characteristics for the PSCs considering the deposition powers of 0, 5, 10, 20, and 30 W.

the deposition power on the QE for the longer wavelength is noticed, which decreases the integrated J_{SC} from 21.34 to 20.80 mA cm^{-2}.

Interestingly, the device's total absorption and reflection are almost the same for all cases, which also confirms the dominating behavior of the ZnO:Cr layer on the optical performance. The description is also confirmed by their complex refractive indices presented in Fig. S1 and published reports in the literature [19,22,56–58]. Moreover, The QE and J_{SC} presented the identical trend of 0 > 5 > 10 > 20 > 30 W. Total QE examination specified once more that an acceptable ETL ensured an important effect of proceeding the photogenerated electron collection and transportation towards the corresponding electrode due to the maximum suitable output with consistency, and surface roughness. This same behavior was also observed by Tsai *et al.* [59]. We additionally investigate a PSC with a thicker ZnO:Cr (500 nm) to further understand the impact of front contact on the PSC's optical performance. The study shows that the thicker ETL significantly drops photon absorption in the active layer, affecting the device's J_{SC} (17.7 mA cm^{-2}) due to increased reflection and parasitic absorption loss due to ZnO:Cr (Fig. S4).

To further understand the effect of optical wave propagation on the device optics, we studied the calculated time-averaged power densities and electric field distribution (EFD) profiles for different incident wavelengths for ZnO:Cr films prepared from different deposition powers. Fig. 5a–e illustrate the investigated PSCs' cross-sectional time-averaged power density plots for an incident wavelength of 350 nm with the deposition powers of 0, 5, 10, 20, and 30 W. Similarly, Fig. 5f–j and k–o demonstrate the power densities for 450 and 700 nm incident wavelengths, respectively. The power densities and EFD plots were determined from the constructive and destructive interferences. For shorter wavelengths (<450 nm), most photons are absorbed by the ZnO:Cr front contact, and a fraction of incident light penetrates to only a few tens of nanometer of the perovskite absorber, as shown in Fig. 5a–j. Noticeably, it is clearly observed that the parasitic losses due to the front contact, which do not contribute to the QE and J_{SC}, get higher with an increment of the Cr doping in ZnO:Cr film. The light with incremental wavelength penetrates the bulk perovskite and is absorbed by the perovskite, whereas almost zero absorption is found in the front ZnO layer. A light with a longer wavelength (700 nm) goes to the back contact and gets reflected; hence, both constructive and destructive wave patterns are formed due to forward and backward propagating waves, as can be understood from the generated fringes of the QE for longer spectrum. However, after

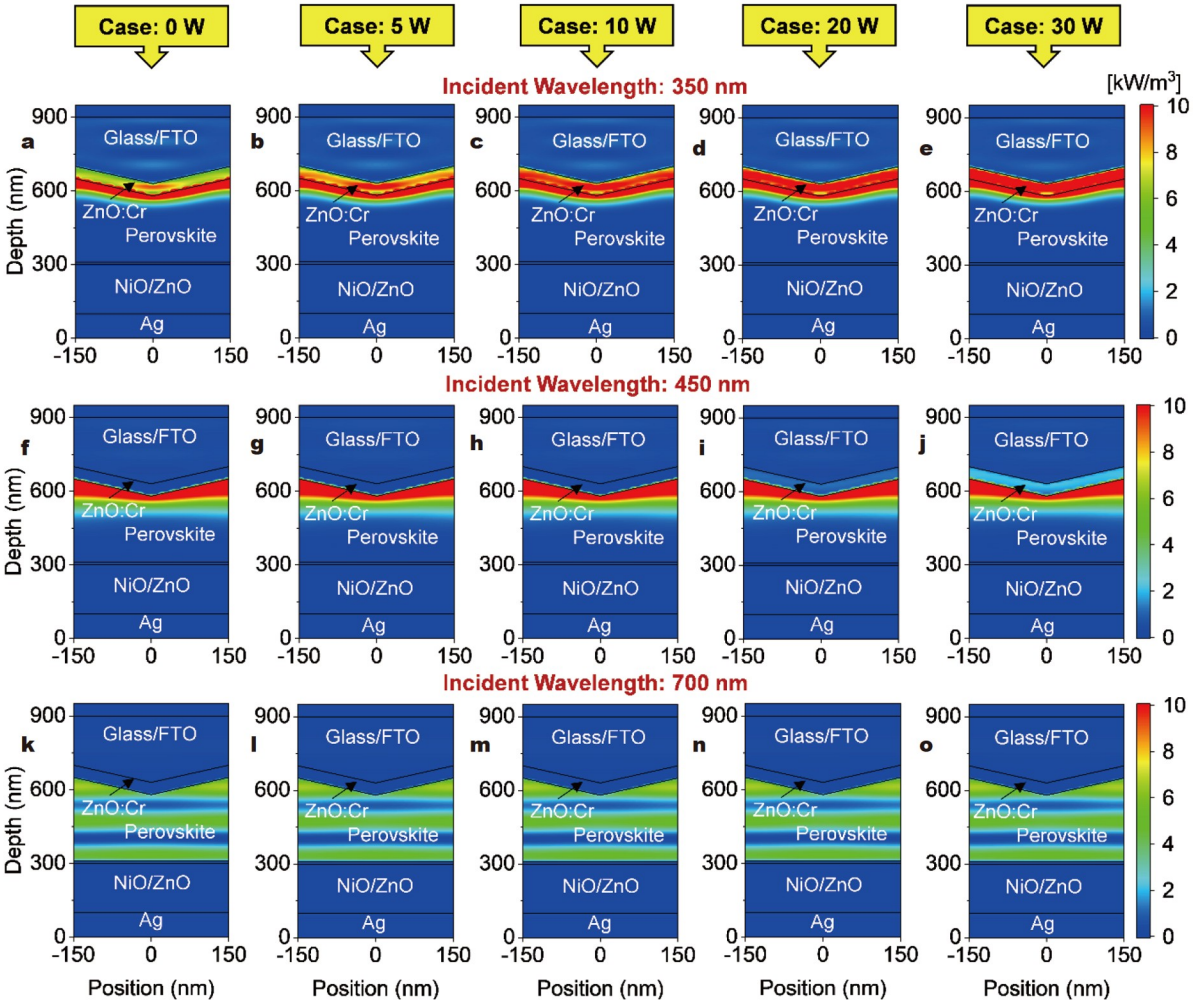

Figure 5 Simulated CR of power density maps at the unit cell's center, under monochromatic wavelengths of (a–e) 350 nm, (f–j) 450 nm, and (k–o) 700 nm for the deposition powers of 0 W (a, f, k), 5 W (b, g, l), 10 W (c, h, m), 20 W (d, i, n), and 30 W (e, j, o), respectively.

800 nm wavelength, close to the perovskite E_g, no absorption (almost zero) occurs in the device. It is also seen that NiO/ZnO HTL has no major absorptions that can increase the parasitic absorption or decrease the QE. This optical phenomenon clearly validates the explanation described by the QE and contact absorption plots shown in Fig. 4a, b. The electromagnetic wave propagations can be further authenticated by the calculated EFDs within the device.

Fig. S5 demonstrates the EFD plots for incident light of 350, 450, and 700 nm for various Cr doping conditions. PSCs' optics clearly shows that the Cr doping in ZnO:Cr front contact affects the QE and J_{SC} substantially. The *J-V* curves of PSCs in superstrate configurations for various deposition powers of ZnO:Cr are shown in Fig. 4d, where the extracted photovoltaic values are summarized in Table 3. The PSC's performance drops by increasing the Cr doping in ZnO:Cr contact. The V_{OC}, J_{SC}, FF, and ECE vary from 1.140 to 1.163 V, 20.90 to 21.51 mA cm^{-2}, 82% to 83%, and 19.5% to 20.5%, respectively. Simulated electrical parameters are equivalent to the experimental outputs, where the experimentally realized best-performance $MAPbI_3$-based PSCs give a maximum V_{OC} and FF of 1.18 V and 86%, individually [60,61]. Hence, it is necessary to maintain the trade-off between doping amount and transparency of the front contact to ensure high efficiency. In this study, we have considered 5 W ZnO:Cr front contact for future investigations as it can fulfill most front contact requirements (e.g., suitable work function, high transmission, and low absorption) [22].

Nanophotonic design of PSCs

Till now, we have studied the superstrate PSC, which not only validates the adapted numerical approach, but also confirms the effect of Cr doping on ZnO:Cr ETL for the realization of efficient devices. Nevertheless, as shown in Fig. 3a, the investigated PSC structure has a planar front surface, limiting solar cell performance due to high optical losses. Reflections at the device's front are mainly responsible for producing such optical losses, limiting the J_{SC} and ECE. Our results show that almost 15% of incident photons are lost due to front reflections, which do not contribute to the J_{SC} of the device. By texturing the solar cell interfaces, photon absorptions can be enhanced; however, it impairs the device's electrical properties [12,14]. Hence, it is indispensable to design a front contact for PSCs that provides efficient photon management and better electrical properties. Thus, we investigate the PSCs in substrate configuration in the remaining section as the superstrate configuration does not prepare a nanotexture front contact. In this study, we propose a PSC embedded with a nanophotonic front contact with an array of ZnO:Cr nanocones, which can be prepared by imprinting and stamping, metal-organic chemical vapor deposition (MOCVD), or lithography techniques or sputtering combined with the wet etching methods [22,62–65]. Fig. 6a depicts the 3D geometries of the nanotextures; however, the period (P), diameter (D), and height (H) of the nanocones have significant influences on the device performance. Preliminary analysis by 3D optical simulations integrated with PSO algorithm confirms that the nanocone diameter has to be equal to the period of the texture [52]. Besides, the continuous ZnO:Cr layer's thickness affects the solar cell performance and stability. The individual layer's thickness is kept constant to the previously studied superstrate PSCs to maintain consistency. A schematic CR of planned PSC is shown in Fig. 6d, where the interfaces between contacts are non-textured, confirming the PSC device's maximum V_{OC} and FF.

The nanocone's profile dimensions D and H are varied from 300 to 600 nm to study optical wave transmission. It is noted that the P is equal to D. Contour plots, as shown in Fig. 6b, c, demonstrate the determination of an optimum point for the textured PSCs, which can give high J_{SC} and low reflections. It is observed that when the diameter is larger than 450 nm and the height is less than 600 nm, the PSC exhibits optimum performance. The QE, J_{SC}, and reflection of PSCs for different diameters and texture heights are shown in Fig. S6. Using PSO algorithm, the nanophotonic front contact is optimized to realize the highest optical performance (e.g., QE, J_{SC}). The optimum combination of the diameter and height in this study is 600 and 450 nm, respectively, which provides a J_{SC} of 23.6 mA cm^{-2}, higher than the J_{SC} values of the devices shown in Fig. S6. The calculated J_{SC} of the texture PSC is 10%–20% higher than the flat devices in superstrate and substrate configurations (Fig. 6h). Such high photon absorptions indicate efficient energy management within the device in terms of improved light incorporation and trapping. The time-average power density profiles of the simulated device show the effects of light incoupling and light trapping to enhance photon absorption in the PSC. Fig. 6e–g present the power densities captivated within the PSC at 350, 450, and 700 nm single wavelength, respectively. It is evident that the photon absorptions are maximized in the case of textured PSC compared with the reference flat device for both shorter (λ = 450 nm) and longer (λ = 700 nm) wavelengths.

Most photons in the shorter wavelengths (UV region) are absorbed by the nanophotonic front contact, as shown in Fig. 6e, which can efficiently minimize the active layer's UV degradation compared with the planar device. The UV response kinetics of the PSC device is the photoexcited carrier's recombination. The carrier recombination possibility (P_{rec}) is intensely connected with UV exposure, especially the PSC device with c-TiO_2 (c stands for compact) ETL since it has been assumed that the degradation starts at the interface of perovskite/TiO_2 [66]. The P_{rec} for c-TiO_2 ETL increases nearly double-fold after the introduction of UV light. This phenomenon specifies that additional photoexcited carrier recombination occurs at the perovskite/c-TiO_2 heterojunction. With inherent oxygen vacancies in high volume in crystalline c-TiO_2, the leading

Table 3 Comparative photovoltaic values deduced from *J-V* curves shown in Fig. 4d

Deposition power	V_{OC} (V)	J_{SC} (mA cm^{-2})	FF (%)	ECE (%)
0 W	1.152	21.51	82.5	20.4
5 W	1.163	21.30	83.0	20.5
10 W	1.154	21.25	82.5	20.2
20 W	1.140	21.10	82.0	19.7
30 W	1.140	20.90	82.0	19.5

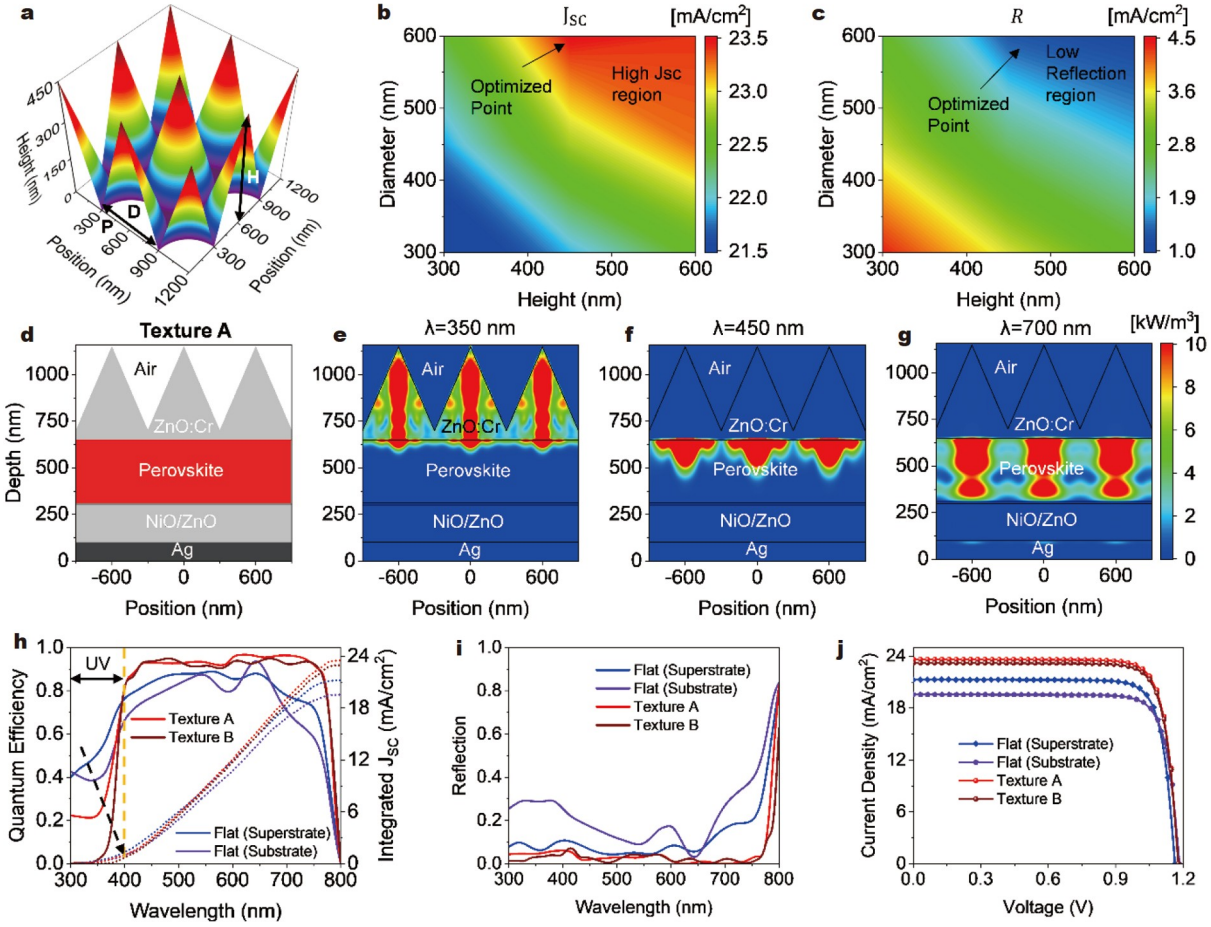

Figure 6 (a) The 3D outline of the front metal oxide cone-shaped nanotexture with the dimension details (Period, *P*; diameter, *D*; and Height, *H*). A comparison of (b) short-circuit current densities, J_{SC} and (c) reflection losses, *R*, while varying the diameter and height of the nanocone texture. (d) A schematic cross-section of the PSC (Texture A) covered with metal-oxide nanocone textures. The optimized nanocone has a *P* of 600 nm, *D* of 600 nm, and *H* of 450 nm. Corresponding simulated time-average power density maps for an incident of (e) 350 nm, (f) 450 nm, and (g) 700 nm light, correspondingly. Comparing the (h) quantum efficiencies, (i) reflections, and (j) *J-V* of flat and textured PSCs. Texture A: the ZnO:Cr continuous layer of 50 nm thick. Texture B: the ZnO:Cr continuous layer of 320 nm thick. The deposition power of 5 W was considered for the preparation of ZnO:Cr film.

recombination pathways seem to be the inter-band uptake of photoexcited charge carrier pairs. However, holes in c-TiO_2 during UV irradiation respond to captivated oxygen radicals, creating a huge volume of unpopulated deep electron trapping sites. This, in turn, seizes the photoexcited electrons generated in the perovskite layer, increasing P_{rec} [67].

Consequently, the V_{OC} and J_{SC} of PSC are highly reduced once illuminated in the UV light, revealing significant deprivation in PCE. Based on the report from Lee *et al.* [66], the FF and J_{SC} were significantly degraded while V_{OC} showed the slightest degradation in a particular 365-nm UV-light exposure for 100 h; as a result, the device lost 65.60% of the initial ECE. However, the photon absorption in the perovskite layer is enhanced with an increase of the incident wavelength until 700 nm (Fig. 6f, g), after that, perovskite absorption decreases till close to the bandgap of the perovskite (λ = 800 nm), where reflections and parasitic absorption at the HTL/metal interface become dominant. The standing wave-like patterns also verify this for shorter wavelengths (e.g., 450 nm), where the nanocones acting like a refractive index gradient lets improved light incoupling contribute to enhanced J_{SC}. For the longer wavelengths (e.g., 700 nm), the standing wave-like patterns in the perovskite layer are formed due to the diffraction of the incident light that allows efficient light trapping, further facilitating improved J_{SC}. The textured devices' optical response can be more certified by corresponding EFD as given in Fig. S7. For comparison, the time-average power density and EFD maps of the reference device in substrate configuration are displayed in Fig. S8. It is noted that a glass cover or polymer coating layer (usually for the encapsulation) is considered at the top of devices while demonstrating a real device. The glass or polymer coating can influence the PSCs' performance in terms of their conversion efficiencies and device stability. Although a glass or polymer coating does not exhibit substantial parasitic losses, it can affect the optics of the complete device due to the difference in the refractive index. We attempted to perform optical simulations for a set of solar cells (planar and nanophotonic configurations) to observe how an encapsulation impacts the device's performance. Simulation results are provided in Fig. S9. Schematic CRs of investigated devices are depicted in Fig. S9a–d, and corresponding absorptions, reflections, QEs, and J_{SC} are presented in Fig. S9e–h. It is observed that the glass layer dramatically influences the optical properties of the flat device, which improves the J_{SC} by almost 1 mA cm^{-2}. Additionally, the glass

layer helps to lower the UV absorption in the active layer; however, it creates an increased number of interference fringes with an improved QE in the longer wavelength region. In the case of textured solar cells, absorptions and reflections of both devices are comparable (Fig. S9g), which leads to an equivalent J_{SC} of ~23.6 mA cm^{-2}, as shown in Fig. S9h. Compared with the solar cell without glass, the QE of the glass-coated device drops in the UV region (<400 nm) and improved in the wavelength range from 400 to 550 nm. The description is nicely matched with our previously published studies [10,16,22,28]. Therefore, it can be summarized that the glass cover or polymer coating layer can influence the optics of the flat device; however, the performance of nanophotonic devices is not significantly affected by the encapsulation or polymer coating layer. Further information on the solar cell's encapsulation is described in Section S2 in the Supplementary Information.

Additionally, to further study the PSC's performance integrated with nanocone front contact, a comparison of QEs and corresponding integrated J_{SC} of planar and textured PSCs is provided in Fig. 6h. Herein, we considered two cases of textured solar cells (Texture A and Texture B). The fundamental difference between these two cases is only the thickness of the ZnO:Cr continuous layer. In Texture A, the ZnO:Cr continuous layer has a thickness of 50 nm that gives the optimum optoelectronic performance. The thickness is increased to 320 nm for Texture B to realize better device stability by comprising the optical performance. The devices possessing textured front contact demonstrate greater QEs through the full visible region of irradiation than that of non-textured one by reducing large interference fringes *via* improved light incoupling and light trapping within the device, as shown in Fig. 6h. As a result, the J_{SC} of the textured PSC is enhanced by ~17% compared with the reference planar solar cell. In addition to that, the optical loss due to reflection is reduced from 15% to only 3%, as illustrated in Fig. 6i. The explanation of these optical enhancements nicely validates the description provided in power density and EFD maps shown in Fig. 6e–g, Figs S7 and S10, respectively. Notably, the textured PSCs reduced photon absorptions in the UV region compared with that of planar devices, which can prevent the degradation of the perovskite layer from excessive UV exposures [68]. In particular, moving from Texture A to Texture B substantially minimizes the perovskite layer's UV absorption.

The calculated power densities and EFD profiles presented in Fig. S10 can confirm the optical wave transmission and absorption mechanism. Texture B structure also enables a more uniform absorption, improving the device's photostability. Their average lateral and depth absorbed power densities confirm the ability to control incident light. A comparison of lateral and depth power densities at the wavelength of 600 nm is presented in Fig. S11. The depth averages maintain the lateral periodicity of 600 nm of the nanocone front contact. Compared with Texture A, less power modulation is observed in the case of Texture B structure, which can provide better thermo- and photo-stability [68]. The lateral and depth average maxima are shifted from ~19 to ~13 kW m^{-3} and from ~7.5 to ~3.5 kW m^{-3}, respectively, while moving from Texture A to Texture B. However, the calculated J_{SC} is reduced by 0.4 mA cm^{-2} in the Texture B. *J-V* characteristics of textured PSCs are presented in Fig. 6j. Information about the corresponding flat devices is also included in the figure for reference. Extracted photovoltaic parameters are summarized in Table 4; noticeably, J_{SC} values determined from the electrical simulations are comparable to the optical simulation results. Texture A PSC exhibits a J_{SC} of 23.6 mA cm^{-2}, V_{OC} of 1.181 V, FF of 83.5%, as well as ECE of 23.3%. In the meantime, Texture B PSC illustrates a J_{SC} of 23.2 mA cm^{-2}, V_{OC} of 1.181 V, FF of 83.5%, and ECE of 22.9%. In contrast, the equivalent non-textured device in substrate configuration reveals a J_{SC} of 19.5 mA cm^{-2}, V_{OC} of 1.183 V, FF of 83.5%, and ECE of 19.2%. These calculated photovoltaic parameters are very competitive to the best PSCs [60,61]. Remarkably, switching from non-textured substrate configuration of the device to the textured one does not depreciate the device's electrical output, confirmed by the recent work on PSCs demonstrated by Wei *et al.* [69]. Hence, it can be concluded that the projected PSC enclosed using nanophotonic metal-oxide-based front contact is appropriate for the realization of the high-performance device in terms of enhanced optoelectronic properties and enhanced photostability since light intensity has a substantial role to regulate perovskite film degradation, for developing future flexible solar cells, and perovskite-based TSC applications. To understand the optics of perovskite/perovskite TSCs, we have studied a TSC covered with the proposed nanophotonic front contact. The thicknesses of the contact layers are kept similar to the single-junction PSC. A wide and a narrow bandgap perovskite active layers are considered as top and bottom cells, respectively, in the tandem structure [13]. A 50-nm-thick SnO_2 layer acts as an interlayer that connects top and bottom cells. The TSC matched with a J_{SC} of 17.9 mA cm^{-2}, with a top cell of 150 nm and a bottom cell of 800 nm thicknesses, separately. The schematic CR of the considered TSC is depicted in Fig. S12a. The QE with J_{SC} of the tandem device is presented in Fig. S12b. Further details on the realization of perovskite-based TSCs are provided in our previous studies [5,10,18].

CONCLUSION

We studied the realization of front contact for efficient PSCs with enhanced UV-stability. The magnetron sputtering technique deposited ZnO:Cr film at ambient temperature. The deposition power was altered from 0 to 30 W, facilitating optimization of the film. The film's structural, morphological, compositional, and optoelectronic properties confirmed the high quality, which allows it to be further utilized as a potential ETL for PSCs. The photovoltaic attributes of the proposed archi-

Table 4 Comparative photovoltaic values deduced from *J-V* curves shown in Fig. 5j

Solar cell type	V_{OC} (V)	J_{SC} (mA cm^{-2})	FF (%)	ECE (%)
Flat (Superstrate)	1.163	21.3	83.0	20.5
Flat (Substrate)	1.183	19.5	83.5	19.2
Texture A	1.181	23.6	83.5	23.3
Texture B	1.181	23.2	83.5	22.9

tectured PSCs were studied by a cutting-edge 3D numerical simulation that provides a relationship between device geometry and material's properties with enhanced efficiency and stability. A 3D FDTD investigated the numerical modeling and optimization (embedded with PSO) algorithm; however, FEM simulations aided in investigating the electrical features of the device. A very good settlement is found amid the results from laboratory prepared and simulated devices, validating the current study's numerical approach. In this part of the current work, an efficient PSC in the superstrate configuration was fabricated at the adjusted circumstance, exhibiting a J_{SC} of 21.1 mA cm^{-2}, V_{OC} of 1.08 V, FF of 76%, and ECE of 17.3%. Furthermore, the influence of Cr content in ZnO:Cr ETL on the device performance was investigated in detail. Then we proposed a PSC device of substrate structure, which is just the reverse of superstrate architecture. The planar device is encapsulated with an array of metal-oxide nanocones, improving the efficiency by reducing optical losses. A detailed optimization process of the nanocone is provided. The nanophotonic front contact allows broadband light incoupling and light trapping, enhancing J_{SC}. Compared with the planar device, the J_{SC} is improved by 17%, reducing reflections by 12%. Furthermore, it is seen that the substrate PSC displays superior photovoltaic attributes besides checking the degradation of the perovskite layer. The light illumination impact on photoinduced instability of the device has been extensively deliberated. The standardized PSC having nanocone front contact exhibits an expected ECE of 23.3%, with a J_{SC} of 23.6 mA cm^{-2}, a V_{OC} of 1.181 V, and an FF of 83.5%. Our cumulative outcomes demonstrate that a simple combination of front nanocones can enhance photostability without significantly compromising the performance of PSCs in the long run. In addition, the anticipated PSC designing strategy is ready to be taken into consideration for implementation as the top cell in perovskite/silicon or perovskite/perovskite TSCs with high efficiencies.

Received 26 November 2021; accepted 18 January 2022; published online 11 March 2022

1 Kojima A, Teshima K, Shirai Y, *et al*. Organometal halide perovskites as visible-light sensitizers for photovoltaic cells. J Am Chem Soc, 2009, 131: 6050–6051
2 Jena AK, Kulkarni A, Miyasaka T. Halide perovskite photovoltaics: Background, status, and future prospects. Chem Rev, 2019, 119: 3036–3103
3 Green MA, Dunlop ED, Hohl-Ebinger J, *et al.* Solar cell efficiency tables (version 56). Prog Photovolt Res Appl, 2020, 28: 629–638
4 Hossain MI, Shahiduzzaman M, Ahmed S, *et al.* Near field control for enhanced photovoltaic performance and photostability in perovskite solar cells. Nano Energy, 2021, 89: 106388
5 Hossain MI, Saleque AM, Ahmed S, *et al.* Perovskite/perovskite planar tandem solar cells: A comprehensive guideline for reaching energy conversion efficiency beyond 30%. Nano Energy, 2021, 79: 105400
6 Kim JY, Lee JW, Jung HS, *et al.* High-efficiency perovskite solar cells. Chem Rev, 2020, 120: 7867–7918
7 Zhang P, Yang F, Kapil G, *et al.* Enhanced performance of ZnO based perovskite solar cells by Nb_2O_5 surface passivation. Org Electron, 2018, 62: 615–620
8 Shahiduzzaman M, Ismail Hossain M, Otani S, *et al.* Low-temperature treated anatase TiO_2 nanophotonic-structured contact design for efficient triple-cation perovskite solar cells. Chem Eng J, 2021, 426: 131831
9 Grätzel M. The light and shade of perovskite solar cells. Nat Mater, 2014, 13: 838–842
10 Hossain MI, Qarony W, Jovanov V, *et al.* Nanophotonic design of perovskite/silicon tandem solar cells. J Mater Chem A, 2018, 6: 3625–3633
11 Li H, Zhang W. Perovskite tandem solar cells: From fundamentals to commercial deployment. Chem Rev, 2020, 120: 9835–9950
12 Sahli F, Werner J, Kamino BA, *et al.* Fully textured monolithic perovskite/silicon tandem solar cells with 25.2% power conversion efficiency. Nat Mater, 2018, 17: 820–826
13 Hossain MI, Shahiduzzaman M, Saleque AM, *et al.* Improved nanophotonic front contact design for high-performance perovskite single-junction and perovskite/perovskite tandem solar cells. Sol RRL, 2021, 5: 2100509
14 Haque S, Alexandre M, Mendes MJ, *et al.* Design of wave-optical structured substrates for ultra-thin perovskite solar cells. Appl Mater Today, 2020, 20: 100720
15 Shahiduzzaman M, Visal S, Kuniyoshi M, *et al.* Low-temperature-processed brookite-based TiO_2 heterophase junction enhances performance of planar perovskite solar cells. Nano Lett, 2019, 19: 598–604
16 Hossain MI, Mohammad A, Qarony W, *et al.* Atomic layer deposition of metal oxides for efficient perovskite single-junction and perovskite/silicon tandem solar cells. RSC Adv, 2020, 10: 14856–14866
17 Hossain MI, Qarony W, Ma S, *et al.* Perovskite/silicon tandem solar cells: From detailed balance limit calculations to photon management. Nano-Micro Lett, 2019, 11: 58
18 Qarony W, Hossain MI, Jovanov V, *et al.* Influence of perovskite interface morphology on the photon management in perovskite/silicon tandem solar cells. ACS Appl Mater Interfaces, 2020, 12: 15080–15086
19 Shahiduzzaman M, Karakawa M, Yamamoto K, *et al.* Interface engineering of compact-TiO_x in planar perovskite solar cells using low-temperature processable high-mobility fullerene derivative. Sol Energy Mater Sol Cells, 2018, 178: 1–7
20 Zhou L, Li X, Ni GW, *et al.* The revival of thermal utilization from the sun: Interfacial solar vapor generation. Natl Sci Rev, 2019, 6: 562–578
21 Haque S, Mendes MJ, Sanchez-Sobrado O, *et al.* Photonic-structured TiO_2 for high-efficiency, flexible and stable perovskite solar cells. Nano Energy, 2019, 59: 91–101
22 Hossain MI, Hongsingthong A, Qarony W, *et al.* Optics of perovskite solar cell front contacts. ACS Appl Mater Interfaces, 2019, 11: 14693–14701
23 Shah AH, Basheer Ahamed M, Neena D, *et al.* Investigations of optical, structural and antibacterial properties of Al-Cr dual-doped ZnO nanostructures. J Alloys Compd, 2014, 606: 164–170
24 Ryu YR, Zhu S, Budai JD, *et al.* Optical and structural properties of ZnO films deposited on GaAs by pulsed laser deposition. J Appl Phys, 2000, 88: 201–204
25 Zardetto V, Williams BL, Perrotta A, *et al.* Atomic layer deposition for perovskite solar cells: Research status, opportunities and challenges. Sustain Energy Fuels, 2017, 1: 30–55
26 Yamauchi Y, Kamakura Y, Isagi Y, *et al.* Study of novel floating-gate oxide semiconductor memory using indium-gallium-zinc oxide for low-power system-on-panel applications. Jpn J Appl Phys, 2013, 52: 094101
27 Yu L, Luo D, Wang H, *et al.* Highly conductive zinc-tin-oxide buffer layer for inverted polymer solar cells. Org Electron, 2016, 33: 156–163
28 Hossain MI, Hasan AKM, Qarony W, *et al.* Electrical and optical properties of nickel-oxide films for efficient perovskite solar cells. Small Methods, 2020, 4: 2000454
29 Hossain MI, Khan HA, Kozawa M, *et al.* Perovskite color detectors: Approaching the efficiency limit. ACS Appl Mater Interfaces, 2020, 12: 47831–47839
30 Cao J, Wu B, Chen R, *et al.* Efficient, hysteresis-free, and stable perovskite solar cells with ZnO as electron-transport layer: Effect of surface passivation. Adv Mater, 2018, 30: 1705596
31 Zhang D, Zhang X, Bai S, *et al.* Surface chlorination of ZnO for perovskite solar cells with enhanced efficiency and stability. Sol RRL, 2019, 3: 1900154
32 Chen R, Cao J, Duan Y, *et al.* High-efficiency, hysteresis-less, UV-stable perovskite solar cells with cascade ZnO-ZnS electron transport layer. J Am Chem Soc, 2019, 141: 541–547
33 Zheng D, Wang G, Huang W, *et al.* Combustion synthesized zinc oxide

electron-transport layers for efficient and stable perovskite solar cells. Adv Funct Mater, 2019, 29: 1900265
34 Liang H, Hu YC, Tao Y, *et al.* Existence of ligands within sol-gel-derived ZnO films and their effect on perovskite solar cells. ACS Appl Mater Interfaces, 2019, 11: 43116–43121
35 Vijayalakshmi K, Sivaraj D. Enhanced antibacterial activity of Cr doped ZnO nanorods synthesized using microwave processing. RSC Adv, 2015, 5: 68461–68469
36 Qarony W, Hossain MI, Tamang A, *et al.* Enhancing the energy conversion efficiency of low mobility solar cells by a 3D device architecture. J Mater Chem C, 2019, 7: 10289–10296
37 Akhtar MJ, Alhadlaq HA, Alshamsan A, *et al.* Aluminum doping tunes band gap energy level as well as oxidative stress-mediated cytotoxicity of ZnO nanoparticles in MCF-7 cells. Sci Rep, 2015, 5: 13876
38 Li SS, Su YK. Improvement of the performance in Cr-doped ZnO memory devices *via* control of oxygen defects. RSC Adv, 2019, 9: 2941–2947
39 Khan HR, Akram B, Aamir M, *et al.* Electronic tuning of zinc oxide by direct fabrication of chromium (Cr) incorporated photoanodes for visible-light driven water splitting applications. Sci Rep, 2020, 10: 9707
40 Ren CY, Chiou SH, Hsue CS. Ga-doping effects on electronic and structural properties of wurtzite ZnO. Phys B-Condensed Matter, 2004, 349: 136–142
41 Kim KJ, Park YR. Optical investigation of $Zn_{1-x}Fe_xO$ films grown on Al_2O_3(0001) by radio-frequency sputtering. J Appl Phys, 2004, 96: 4150–4153
42 Haja Hameed AS, Karthikeyan C, Sasikumar S, *et al.* Impact of alkaline metal ions Mg^{2+}, Ca^{2+}, Sr^{2+} and Ba^{2+} on the structural, optical, thermal and antibacterial properties of ZnO nanoparticles prepared by the co-precipitation method. J Mater Chem B, 2013, 1: 5950
43 Hosseini SM, Sarsari IA, Kameli P, *et al.* Effect of Ag doping on structural, optical, and photocatalytic properties of ZnO nanoparticles. J Alloys Compd, 2015, 640: 408–415
44 Shan FK, Shin BC, Jang SW, *et al.* Substrate effects of ZnO thin films prepared by PLD technique. J Eur Ceramic Soc, 2004, 24: 1015–1018
45 Young DL, Williamson DL, Coutts TJ. Structural characterization of zinc stannate thin films. J Appl Phys, 2002, 91: 1464–1471
46 Wang S, Bo W, Zhong M, *et al.* Effect of Cr content on the properties of magnetic field processed Cr-doped ZnO-diluted magnetic semiconductors. J Nanomaterials, 2012, 2012: 1–7
47 Bylsma RB, Becker WM, Kossut J, *et al.* Dependence of energy gap on x and T in $Zn_{1-x}Mn_xSe$: The role of exchange interaction. Phys Rev B, 1986, 33: 8207–8215
48 Cheng W, Ma X. Structural, optical and magnetic properties of Fe-doped ZnO. J Phys-Conf Ser, 2009, 152: 012039
49 Rajachidambaram JS, Sanghavi S, Nachimuthu P, *et al.* Characterization of amorphous zinc tin oxide semiconductors. J Mater Res, 2012, 27: 2309–2317
50 Abzieher T, Moghadamzadeh S, Schackmar F, *et al.* Electron-beam-evaporated nickel oxide hole transport layers for perovskite-based photovoltaics. Adv Energy Mater, 2019, 9: 1802995
51 Qarony W, Hossain MI, Salleo A, *et al.* Rough *versus* planar interfaces: How to maximize the short circuit current of perovskite single and tandem solar cells. Mater Today Energy, 2019, 11: 106–113
52 Shahiduzzaman M, Hossain MI, Visal S, *et al.* Spray pyrolyzed TiO_2 embedded multi-layer front contact design for high-efficiency perovskite solar cells. Nano-Micro Lett, 2021, 13: 36
53 Niu G, Li W, Meng F, *et al.* Study on the stability of $CH_3NH_3PbI_3$ films and the effect of post-modification by aluminum oxide in all-solid-state hybrid solar cells. J Mater Chem A, 2014, 2: 705–710
54 Heo JH, Im SH, Noh JH, *et al.* Efficient inorganic-organic hybrid heterojunction solar cells containing perovskite compound and polymeric hole conductors. Nat Photon, 2013, 7: 486–491
55 Xing G, Mathews N, Sun S, *et al.* Long-range balanced electron- and hole-transport lengths in organic-inorganic $CH_3NH_3PbI_3$. Science, 2013, 342: 344–347
56 Deng K, Li L. Optical design in perovskite solar cells. Small Methods, 2020, 4: 1900150
57 Kim J, Kim KS, Myung CW. Efficient electron extraction of SnO_2 electron transport layer for lead halide perovskite solar cell. npj Comput Mater, 2020, 6: 100
58 Liu J, Wang G, Luo K, *et al.* Understanding the role of the electron-transport layer in highly efficient planar perovskite solar cells. ChemPhysChem, 2017, 18: 617–625
59 Tsai CH, Lin CM, Kuei CH. Investigation of the effects of various organic solvents on the PCBM electron transport layer of perovskite solar cells. Coatings, 2020, 10: 237
60 Chiang CH, Wu CG. A method for the preparation of highly oriented $MAPbI_3$ crystallites for high-efficiency perovskite solar cells to achieve an 86% fill factor. ACS Nano, 2018, 12: 10355–10364
61 Wang Y, Liang Y, Zhang Y, *et al.* Pushing the envelope: Achieving an open-circuit voltage of 1.18 V for unalloyed $MAPbI_3$ perovskite solar cells of a planar architecture. Adv Funct Mater, 2018, 28: 1801237
62 Forin CC, Purica M, Budianu E, Schiopu P. p-NiO/ITO transparent heterojunction—Preparation and characterization. In: 2012 International Semiconductor Conference (CAS 2012), IEEE. Dresden-Grenoble, 2012. 131–134
63 Wang JY, Lee CY, Chen YT, *et al.* Double side electroluminescence from p-NiO/n-ZnO nanowire heterojunctions. Appl Phys Lett, 2009, 95: 131117
64 Ma P, Xu Z, Wang M, *et al.* Fast fabrication of TiO_2 hard stamps for nanoimprint lithography. Mater Res Bull, 2017, 90: 253–259
65 Kang SM, Jang S, Lee JK, *et al.* Moth-eye TiO_2 layer for improving light harvesting efficiency in perovskite solar cells. Small, 2016, 12: 2443–2449
66 Lee SW, Kim S, Bae S, *et al.* Enhanced UV stability of perovskite solar cells with a SrO interlayer. Org Electron, 2018, 63: 343–348
67 Leijtens T, Eperon GE, Pathak S, *et al.* Overcoming ultraviolet light instability of sensitized TiO_2 with meso-superstructured organometal tri-halide perovskite solar cells. Nat Commun, 2013, 4: 1–8
68 Wei J, Wang Q, Huo J, *et al.* Mechanisms and suppression of photo-induced degradation in perovskite solar cells. Adv Energy Mater, 2021, 11: 2002326
69 Wei J, Xu RP, Li YQ, *et al.* Enhanced light harvesting in perovskite solar cells by a bioinspired nanostructured back electrode. Adv Energy Mater, 2017, 7: 1700492

Acknowledgements We acknowledge the Universiti Kebangsaan Malaysia, Malaysia for financial support through the Long-term Research Grant Scheme (LRGS/1/2019/UKM-UKM/6/1). The authors extend their appreciation to Researchers Supporting Project number (RSP-2021/34), King Saud University, Riyadh, Saudi Arabia. This study was also reinforced by a contribution from the Innovation and Technology Commission of Hong Kong (Project No. GHP/040/19SZ).

Author contributions Hasan AKM drafted the original manuscript, prepared the thin film samples, and did the formal analysis with the support of Akhtaruzzaman M and Islam MA. Hossain MI, Tsang YH, and Shahiduzzaman M revised the manuscript, conducted the device modeling and simulations, and fabricated the solar cells. Mohammad G, Akhtaruzzaman M, and Tsang YH are responsible for funding the project. Sopian K was responsible for the overall project administration. All authors contributed to the validation, data curation, revision, and general discussion.

Conflict of interest The authors declare that they have no conflict of interest.

Supplementary information Supporting data are available in the online version of the paper.

Md. Akhtaruzzaman (Senior Member, IEEE) received his PhD degree from the Institute for Molecular Science (IMS), Okazaki, Japan, in March 2003. He is currently serving in the Solar Energy Research Institute (SERI) of Universiti Kebangsaan Malaysia (UKM) in Malaysia. His research interests include the rational design of organic/inorganic semiconductors, nano-materials and device physics for various organic electronic device applications.

Mohammad Ismail Hossain earned his PhD degree (AP) from The Hong Kong Polytechnic University (PolyU) with a prestigious fellowship. He is currently working as a Postdoctoral Research Scientist at the University of California, Davis, USA attached with the Berkeley Nanolab. He was a Postdoctoral Fellow at the City University of Hong Kong and a Research Associate at PolyU. His research focuses on optics, thermophotovoltaics, perovskite-based high-efficiency solar cells, multispectral-image sensors, and thin-film materials.

A. K. Mahmud Hasan received his PhD degree in renewable energy from SERI, Universiti Kebangsaan Malaysia. His areas of expertise and interest are on the rational design of organic/inorganic semiconductors, nano-materials for various applications, including dye-sensitized solar cells (DSSCs), perovskite thin film solar cells, nano-electronics and electroluminescence devices. Currently he is focusing on the green synthesis of inorganic semiconductor materials for the third generation photovoltaic and sensor devices.